Soliton dynamics in a piecewise gas-filled hollow-core fiber for efficient dispersive wave emission in the vacuum-ultraviolet range

Ding Wang* and Yuxin Leng†

State Key Laboratory of High Field Laser Physics and CAS Center for Excellence in Ultra-intense Laser Science, Shanghai Institute of Optics and Fine Mechanics (SIOM), Chinese Academy of Sciences (CAS), Shanghai 201800, China

(Received 17 August 2022; accepted 15 November 2022; published 28 November 2022)

Table-top coherent vacuum-ultraviolet (VUV) sources are important in many researches. Dispersive wave (DW) emission in a gas-filled hollow-core fiber (HCF) is an efficient way to obtain tunable VUV source with microjoule-level pulse energy. However, the shortest VUV wavelength is limited above 110 nm. This work investigated a method using a piecewise HCF in order to push the shortest VUV DW emission below 110 nm efficiently. The rich and complex spatiotemporal soliton dynamics in the HCF is revealed through rigorous numerical simulations and quantitative analysis. It is found that both the generation of VUV light below 110 nm and the overall conversion efficiencies below 150 nm can be significantly improved if the piecewise gas-filled HCF system is properly designed. As a result, the whole VUV spectrum (200–100 nm) can now be accessed efficiently, with single pulse energy of microjoule level. Different from other widely used intense VUV sources, this source has broad spectrum along with femtosecond time width. These unique characteristics in the VUV spectrum can lead to new research opportunities in various areas.

DOI: 10.1103/PhysRevA.106.053520

I. INTRODUCTION

Vacuum ultraviolet (VUV, 200–100 nm) lights have single photon energies large enough to induce electric transitions or ionizations of outer-shell electrons of most atoms, and therefore play vital roles in research areas such as molecular photochemistry, photodissociation dynamics, interstellar chemistry, and so on [1–3]. Traditionally, VUV light can be obtained through electron-impact excitation in a gas discharge [4]. However, the light is not coherent and therefore not efficient in many applications. Coherent VUV sources have been developed along different paths over the last several decades. One path is based on large-scale facilities such as synchrotron radiation (SR) [5] and free-electron lasers (FEL) [6]. While the merits of these sources include very high brightness, wavelength tunability over a large range, and high spectral resolution, the need for a dedicated facility limits applicability of this method to only a few sites.

Table-top coherent VUV sources include a variety of forms. Excimer lasers [7] are commercially available and used in many industrial applications. But they are not wavelength tunable. Nonlinear frequency conversion in solid crystals can output wavelengths in the VUV range, but is still limited to above 150 nm [8]. The most widely used table-top coherent VUV sources are based on four wave mixing (FWM) using two or three laser beams in a gas cell [9]. By changing the wavelength of one beam, it is possible to tune the VUV wavelength. Noble gases are frequently used as the nonlinear media because they are environmentally friendly and have rich electronic energy-level structures which facilitate multiple ways of frequency mixing [10]. Other gas media such as mercury (Hg) vapor can also be used for VUV radiation and can lead to very high intensity through resonance-enhanced FWM [11].

Recently, by coupling a 10-fs pulse with hundreds of microjoules into a hollow-core fiber (HCF) filled with helium gas Travers *et al.* [12–14] obtained coherent VUV light through a mechanism called dispersive wave (DW) emission. Similar phenomena were also observed previously in many other waveguide systems [15–19], but the energy level is orders of magnitude lower. The energy conversion efficiency (CE) from the driving pulse is over 0.5%, and the single VUV pulse is above microjoule level which is a prerequisite for most applications. The wavelength can be tuned continuously from 110 to 200 nm and above. Different from FEL VUV light and other widely used table-top VUV sources, the VUV source based on a gas-filled HCF has a broad spectrum along with femtosecond time width. These characteristics in the VUV range may lead to new research opportunities in various areas.

However, the problem that the reported tunable range stops at 110 nm is yet to be resolved, because the full potential of a gas-filled HCF is limited by the absorption of the gas medium, and for the helium atom the first sharp absorption edge occurs at 50.4 nm [20], much shorter than 110 nm. Although in practice the lack of suitable gas cell window materials limits the tuning range to longer than 110 nm, numerical simulations show that it is also difficult to obtain VUV below 110 nm efficiently with this method itself. The difficulty in obtaining VUV light shorter than 110 nm is the phase-matching (PM) condition. DW emission can also be explained as a cascaded FWM process involving wavelengths at both sides of the zero-dispersion wavelength (ZDW) in the waveguide to achieve PM [21]. The wavelength tunability of DW emission

*wangding@siom.ac.cn
†lengyuxin@siom.ac.cn

mainly comes from the dispersion change by adjusting the gas pressure. The shorter the wavelength is, the steeper the dispersion curve of the gas medium becomes, which makes PM difficult. Although reducing gas pressure favors the PM at shorter wavelengths, it also lowers the nonlinear refractive index, resulting in little DW emission. Further increasing the driving pulse energy does not compensate for the low nonlinearity. By using a HCF with smaller core, the waveguide dispersion can offset some of the gas dispersion, but it induces larger propagation loss and stops the self-compression process which precedes the DW emission. Therefore, DW emission below 110 nm is not efficient with the current system configuration.

The fact that the whole process can be divided into two stages, i.e., the self-compression process followed by DW emission process, suggests that we can use different system parameters for the two stages. A similar idea that separates the whole process into pulse compression and DW emission stages has been implemented to demonstrate a compact footprint for DW emission [22,23], although no self-compression is utilized. In this work, we propose a different method, i.e., a piecewise HCF, in order to push the shortest VUV DW emission below 110 nm. A piecewise HCF is a single HCF consisting of multiple segments with different core sizes. Compared with separated cascaded HCF systems, an advantage of the piecewise HCF is that the pulse does not need to leave one HCF and be refocused into the following HCF. This not only greatly simplifies the system configuration, but it also make the transfer of a delicate spatiotemporal profile from one stage to the next stage easy, such as the attosecond optical pulses. The number of segments can be easily scaled up, offering much flexibility to tune the dispersion of HCF. This method, if workable, will introduce a new degree of freedom in designing a gas-filled HCF system that already finds applications in delivering high-quality sources from soft x rays to mid-IR wavelengths [24–26]. In this work, we explore these problems through rigorous numerical simulations and quantitative analysis, trying to find the optimal conditions in the large parameter space and revealing the underlying soliton dynamics. According to the results, both the generation of wavelengths below 110 nm and the overall conversion efficiencies below 150 nm can be significantly improved if the piecewise gas-filled HCF system is properly designed. As a result, the whole VUV spectrum (200–100 nm) can now be accessed efficiently, with a single pulse energy of microjoule level. Furthermore, due to the relatively low driving pulse energy (less than 1 mJ) compared with traditional table-top VUV sources (using driving lasers of multiple tens of millijoules), the repetition rate can be increased to hundreds of kilohertz with current fiber lasers [27]. This unique source can have a great impact on the relevant researches involving VUV light.

The rest of the paper is organized as follows. Section II describes the methods used in this research, including the general system configuration and theoretical model. Section III presents the results in two parts. The first part demonstrates the generation of VUV light below 110 nm with efficiency up to 0.3% and single pulse energy above 1 μJ. The second part demonstrates that the conversion efficiency below 150 nm can be increased by more than 200%. This work is mainly interested in the VUV spectrum below 150 nm since there are few methods to obtain high-quality sources in this wavelength range. Section IV discusses the problem of fiber clad damage and a simple method to make the piecewise HCF. The paper ends with a conclusion in Sec. V.

II. METHODS

To make the simulation results comparable with reported experimental results [12], we use similar system setups. A 10-fs pulse at 800 nm is coupled into a piecewise HCF filled with static helium gas. The first HCF segment is 250 μm in core diameter and is intended for the self-compression process. The second segment with a smaller diameter is for DW emission. The total length of the two segments is 3 m. When the beam passes the connection of the segments, the peripheral part will be lost due to the smaller following core. The major problem is to find, if there are any, the optimal size of the second core and the location of the segments' connection for desirable outputs. Tunable experimental conditions also include input pulse energy and gas pressure.

As for the numerical simulations, this work uses a model that directly resolves the spatiotemporal fields in the HCF instead of mode-expansion model, and thus provides some convenience in simulating multisegment propagation. The pulse propagation dynamics in the gas core is described by the generalized unidirectional pulse propagation equations with lossy boundary conditions (gUPPE-b-b) [28–30]:

$$\partial_z E(z,r,\omega) = i\left(\sqrt{\hat{L}} - \frac{\omega}{v_g}\right)E(z,r,\omega) + \frac{\omega}{2\beta c^2}\left[i\omega\frac{P(z,r,\omega)}{\varepsilon_0} - \frac{j(z,r,\omega)}{\varepsilon_0}\right], \quad (1)$$

where $E(z,r,\omega)$ is the pulse in frequency domain; linear operator $\hat{L} = \omega^2\varepsilon(\omega)/c^2 + \Delta_\perp$ describes both the dispersion and diffraction effects; v_g is the velocity of the moving frame; $\beta = \omega n(\omega)/c$ is the frequency-dependent wave number; $P(z,r,\omega)$ and $j(z,r,\omega)$ are the nonlinear polarizations related to bounded and free electrons respectively; ω, c, and ε_0 are angular frequency, light speed, and vacuum permittivity respectively. For the cubic Kerr effect, the nonlinear polarization in the time domain is $P/\varepsilon_0 = \frac{8}{3}n_0 n_2 E^3$ which includes harmonic generation. The gas ionization effect is modeled by $j(t)/\varepsilon_0 = cn_0\eta W(\mathcal{I})U_i(\rho_{nt} - \rho)E/\mathcal{I}$, where $W(\mathcal{I})$ is the ionization rate calculated according to the Perelomov, Popov, and Terent'ev (PPT) model [31], and $\mathcal{I}$ is the pulse intensity envelope; U_i is the ionization potential; ρ is electron density; ρ_{nt} is the gas density. The plasma effect is modeled by $j(\omega)/\varepsilon_0 = \frac{\tau_c(1+i\omega\tau_c)}{1+\omega^2\tau_c^2}\frac{e^2}{\varepsilon_0 m_e}\mathrm{FFT}[\rho E]$, where e, m_e, τ_c are the electron charge, mass, and collision time, respectively. FFT$[\cdots]$ is the Fourier transform. Assuming the ionized electrons are born at rest, the density ρ evolves as

$$\frac{\partial\rho}{\partial t} = W(\mathcal{I})(\rho_{nt} - \rho) + \frac{\sigma\rho\mathcal{I}}{U_i}, \quad (2)$$

where σ is the impact ionization cross section.

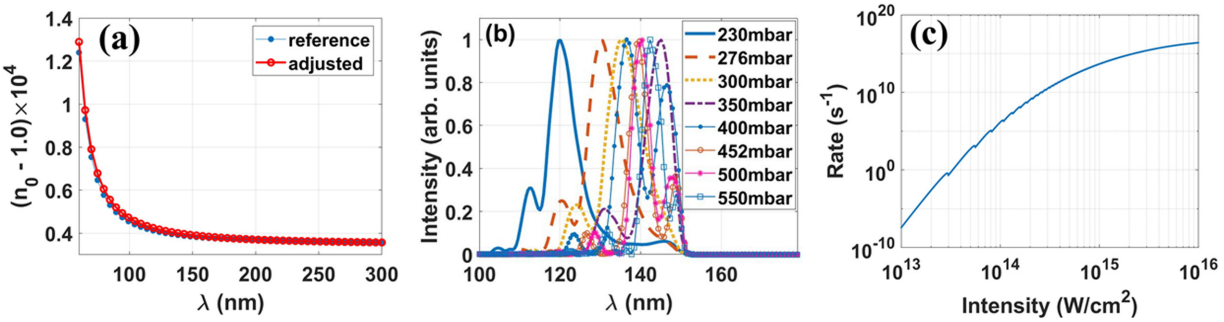

FIG. 1. (a) Comparison of linear refractive index of helium used in the simulations and in Ref. [34]; (b) spectra of the VUV below 150 nm at different pressures. A numerical filter is used to obtain wavelengths below 150 nm. (c) Ionization rate of helium gas according to PPT model.

The boundary condition from the gas core to the fiber clad is

$$E_{\text{boundary}} = \frac{1}{2}\left(\frac{(3+2ik_o\Delta r/n_{\text{clad}}^2)}{9+4k_o^2\Delta r^2/n_{\text{clad}}^4} + \frac{(3+2ik_o\Delta r)}{9+4k_o^2\Delta r^2}\right) \times (4E_1 - E_2), \quad (3)$$

where E_1 and E_2 are fields at Δr and $2\Delta r$ away from the boundary of the hollow core [28]; $k_o = \frac{\omega}{c}\sqrt{n_{\text{clad}}^2 - 1}$, and n_{clad} is the linear refractive index of the fused silica. The complex refractive index of silica glass in the ultraviolet wavelength range is from [32]. This work assumes a straight HCF. Therefore, no bending loss is considered in the model.

The initial pulse takes the following form:

$$E(z=0,t,r) = E_0 \exp\left\{-\frac{r^2}{w_0^2}\right\} \exp\left\{-\frac{t^2}{2t_0^2}\right\} \cos(\omega t), \quad (4)$$

where the optimal coupling condition for the linear polarized Gaussian pulse is $w_0 = 0.65a$, where a is the inner radius of the HCF. To simulate propagation dynamics in a piecewise HCF, the spatiotemporal field at the end of the first segment is interpolated on the numerical grid of the second HCF segment, and the field outside the second core is discarded. The above equations are integrated with self-adaptive step lengths to ensure a well-controlled propagation accuracy.

The parameters used in the simulations are also calibrated with reported experimental data [12]. The linear refractive index of helium is tuned so that the central wavelength of the generated VUV radiation matches the experimental measurement at 230 mbar pressure, as shown in Fig. 1(a). Then the nonlinear refractive index n_2 is adjusted so that the energy conversion efficiencies below 150 nm match experimental results at specific pressures, as listed in Table I. The tunable spectra of the VUV filtered below 150 nm is shown in Fig. 1(b). Changing values of n_2 at different gas pressures do not reflect special physical insights. They only correspond to experimental measurements which are affected by various factors. However, with this calibration systematic errors in the simulations due to improper parameters can be reduced. Figure 1(c) shows the ionization rate of helium according to the PPT model.

Although the numerical model is well established, and the experimental DW spectral range and energy conversion efficiencies are approximately reproduced under different conditions, it should be pointed out that the numerical simulations do not reproduce the mode distribution of DW emission from experimental data under certain conditions. According to [33], the modes below 150 nm in experimental measurements are all EH_{11}, while the numerical simulations show that at pressures between 452 and 550 mbar the dominant modes below 150 nm are EH_{12}. This discrepancy is unclear, and needs to be further investigated. In the following sections, all analyses and conclusions will be based on comparison between the numerical simulations alone.

III. RESULTS

A. Generating VUV light below 110 nm

The main results of numerical experiments are summarized in Fig. 2. The gas pressure is set at 230 mbar. When the connection location between two segments is at 240 cm and the input pulse energy is 426 μJ, the energy conversion efficiency is optimal with core size between 100 and 150 μm for the second HCF [Fig. 2(a)]. Figure 2(d) shows the change of transverse-integrated VUV spectra $\int_0^a rI(\omega, r)dr$ with different core sizes. When the core is larger than 100 μm, both the ZDW and the VUV spectra shift to longer wavelengths with the increase of core sizes. When the core is smaller than 100 μm, the VUV spectrum stops shifting to shorter wavelengths although the ZDW is even shorter. This is because of too large wave guide losses that prevent DW building up over long distances.

TABLE I. Nonlinear refractive index used in the simulations and the energy conversion efficiencies for VUV below 150 nm.

Pressure (mbar)	n_2 (μm^2/TW/bar)	Efficiency[a] (%)	Efficiency[b] (%)
230	0.58	0.55	0.5
276	0.48	0.75	0.8
300	0.44	0.83	0.9
350	0.38	0.95	1.0
400	0.39	1.1	1.2
452	0.41	1.4	1.4
500	0.45	1.7	1.6
550	0.46	1.8	1.8

[a]This work.
[b]Reference [12].

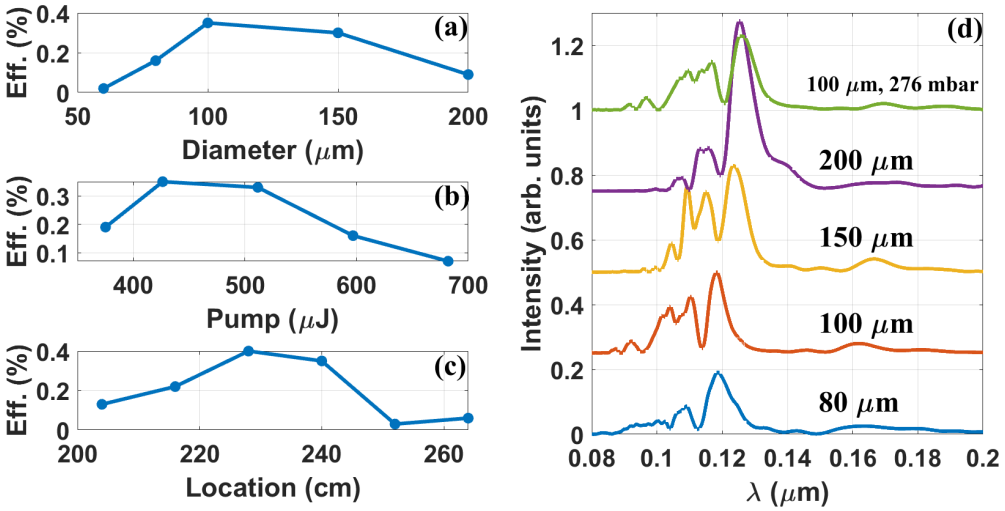

FIG. 2. Conversion efficiencies of VUV light below 110 nm versus (a) core sizes of the second HCF under the conditions of 230 mbar helium pressure, 426 μJ input pulse energy, and joint location at 240 cm; (b) energy of input pulse under the conditions of 230 mbar helium pressure, 100 μm core size for the second HCF, and joint location at 240 cm; (c) location of the starting point of the second HCF under the conditions of 230 mbar helium pressure, 426 μJ input pulse energy, and 100 μm core size for the second HCF. (d) Spectra of the DW VUV emission with different core sizes for the second HCF.

Figure 3(a) shows a typical evolution of transverse-integrated temporal intensity with 100-μm core size for the second segment. The input 10-fs pulse undergoes self-compression and builds up a supercontinuum extending below 300 nm in the first segment of 240 cm length. At this location, the spectrum already covers the ZDW of 334 nm. If the pulse continues to propagate in the 250-μm-core HCF, DW emission centered at 120 nm will build up. After transfer to the second segment, the ZDW shifts to 227 nm, and the pulse experiences a very difference dispersion profile. DW emission centered around 105 nm has more favorable PM conditions. Although it is only 15 nm shorter, the difference in frequency domain is quite large because the central wavelength is very short.

Due to increased anomalous dispersion and high intensity, a large acceleration of the pulse in time domain is observed in the second segment. This is caused by photoionization in the anomalous dispersion regime [18] which leads to soliton self-frequency blueshift. As can be seen in Fig. 3(b), the spectral range below 550 nm is accelerated in the time domain while the longer wavelengths remain fixed in the retarded-frame reference. In the first several centimeters of the second segment, the peak intensity can approach 1.0×10^{15} W/cm^2, and the gas medium is fully ionized. This is partly due to the numerical settings, as the field is simply cropped when the pulse enters the second segment. Diffraction effects enhance the peak intensity at particular locations. However, due to significant self-compression the peak intensity even increases during propagation despite energy losses. The pulse duration (full width at half maximum) is 0.9 fs before entering the second segment with peak intensity 6.2×10^{14} W/cm^2, while the pulse energy is only 30% of the input.

The cropping by the second segment blocks about 85 μJ of the pulse. The HCF clad can be damaged by the high intensity of the beam's peripheral part. This will be discussed in the following section. Despite these disadvantages, the benefit is that the energy from 110 to 90 nm increases substantially in the second segment compared with in the first segment, while from 110 to 330 nm the energy increases in the first segment, but suffers a blocking loss and then decreases continuously in the second segment, as shown in Fig. 3(c).

To reveal the underlying dynamics, the spatiotemporal field can be projected onto different modes. According to mode analysis, the propagation dynamics in the second segment can be divided roughly into three stages. In the first stage, several high-order modes are excited, and the pulse undergoes drastic spatiotemporal transformation accompanied by a large variation of peak intensities. During this process, the energy below 110 nm oscillates with propagation distance as shown in Fig. 3(d), indicating the importance of phase matching in VUV conversion. The first stage lasts several centimeters, after which the fundamental mode dominates and the propagation enters the second stage. In the second stage, the peak intensity is still above the initial input level. Therefore, the soliton process can be driven effectively, and the increase of VUV conversion is fast. When the peak intensity decreases below the input level, the conversion speed also slows down in the third stage. The energy gains below 110 nm only occur in the fundamental mode. The residual high-order modes mainly come from the first stage, and remain almost constant due to negligible wave guide loss. As a result, a VUV pulse covering 90–110 nm is generated with more than 1 μJ energy and a high-quality spatial mode. According to Fig. 3(b), this pulse is about 10 fs.

The input-pulse energy in the above situation is 426 μJ. The optimal energy is found between 426 and 512 μJ [Fig. 2(b)] under the conditions of 230 mbar pressure, 100 μm core size for the second HCF and joint location at 240 cm. If the energy is above this range, the plasma influence in the first segment will be strong enough to split the leading and trailing parts of the 10-fs pulse before the pulse self-compresses as a whole. The leading part is blueshifted, self-compressed, and temporally accelerated away from the trailing part. Although it can be equivalent to a single pulse undergoing the soliton

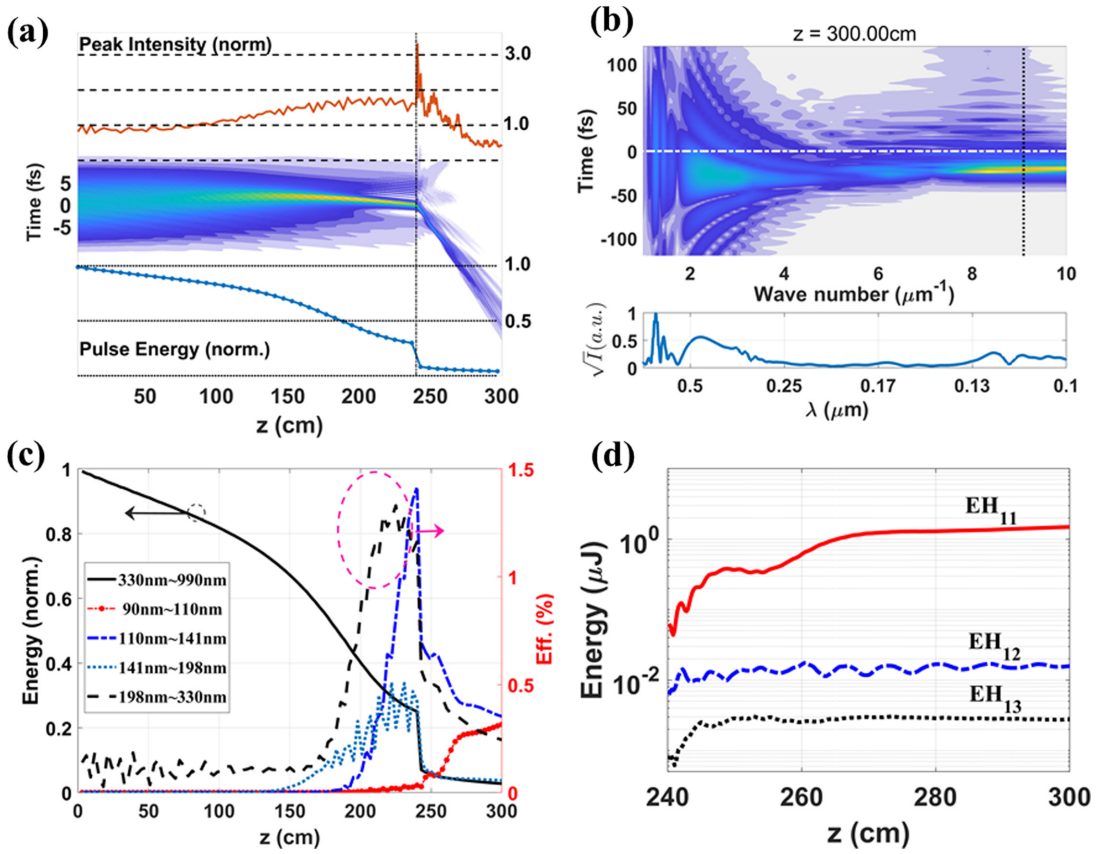

FIG. 3. (a) Evolution of temporal intensity profile, peak intensity (solid line above) and pulse energy (solid-dotted line below) along the piecewise HCF. The peak intensity is normalized with 3.86×10^{14} W/cm^2; the pulse energy is normalized with 426 μJ. (b) Time-frequency distribution of the pulse at the end of the HCF along with the full spectrum (solid line below). The black-dotted line indicates 110 nm. (c) Evolution of energies in different spectral bands along the piecewise HCF. The different wavelength bands have the same frequency interval. The energy of the band from 330 to 990 nm is normalized with 426 μJ; the other bands are represented by conversion efficiencies from the 426-μJ input pulse in percentage. (d) Evolution of mode energies for VUV light below 110 nm in the second HCF segment. The mode components are obtained by projecting the spatiotemporal field on the corresponding mode profiles. The energies are normalized with initial value at the start of the second segment.

process, the pulse energy is reduced, and therefore the VUV conversion efficiency is low.

For the above situation with 426 μJ input energy, 230 mbar pressure, and 100 μm core size for the second HCF, the optimal location of the connection is found between 225 and 240 cm along the propagation [Fig. 2(c)]. According to Fig. 3(c), this location is where the band from 140 to 330 nm reaches the highest conversion efficiency. Note that this band happens to be in the normal dispersion regime (ZDW = 334 nm). This may suggest the direct energy source for 90–110 nm band is from 140 to 330 nm.

Gas pressure is often used to tune the central wavelength of DW emission. When the pressure in the above situation is increased from 230 to 276 mbar, the shortest VUV wavelength will increase about 5 nm, and the conversion efficiency below 110 nm will drop to 0.2%.

In summary, under optimal conditions the conversion efficiency below 110 nm is about 0.3%, and the pulse energy is over 1 μJ. The optimal conditions of the core size, connection location, input pulse energy, and gas pressure have enough tolerance that can be easily achieved in experiment. On the other hand, all the system parameters need to be properly matched in order to achieve optimal performance. This necessitates a careful simulation design according to the parameters of driving lasers.

The piecewise HCF has been shown to obtain VUV radiation with shortest wavelengths. It can also be applied to enhance conversion efficiency for other longer wavelengths. The next section shows the enhancement of the radiation below 150 nm which has few options to obtain efficiently.

B. Improving conversion efficiency below 150 nm

As shown in Table I, VUV below 150 nm can be obtained with gas pressures up to 550 mbar when 341-μJ/10-fs pulses are coupled into the 3-m-long HCF with 250 μm core size. The performance of the piecewise HCF is also tested at pressures between 300 and 550 mbar for comparison. Both the input pulse energy and the core size of the first segment HCF are the same. According to the simulation results, it is found that significant enhancements occur at high pressures, such as 500 and 550 mbar. At both pressures, the enhancement can be more than 200%, which amounts to a pulse energy of more than 15 μJ.

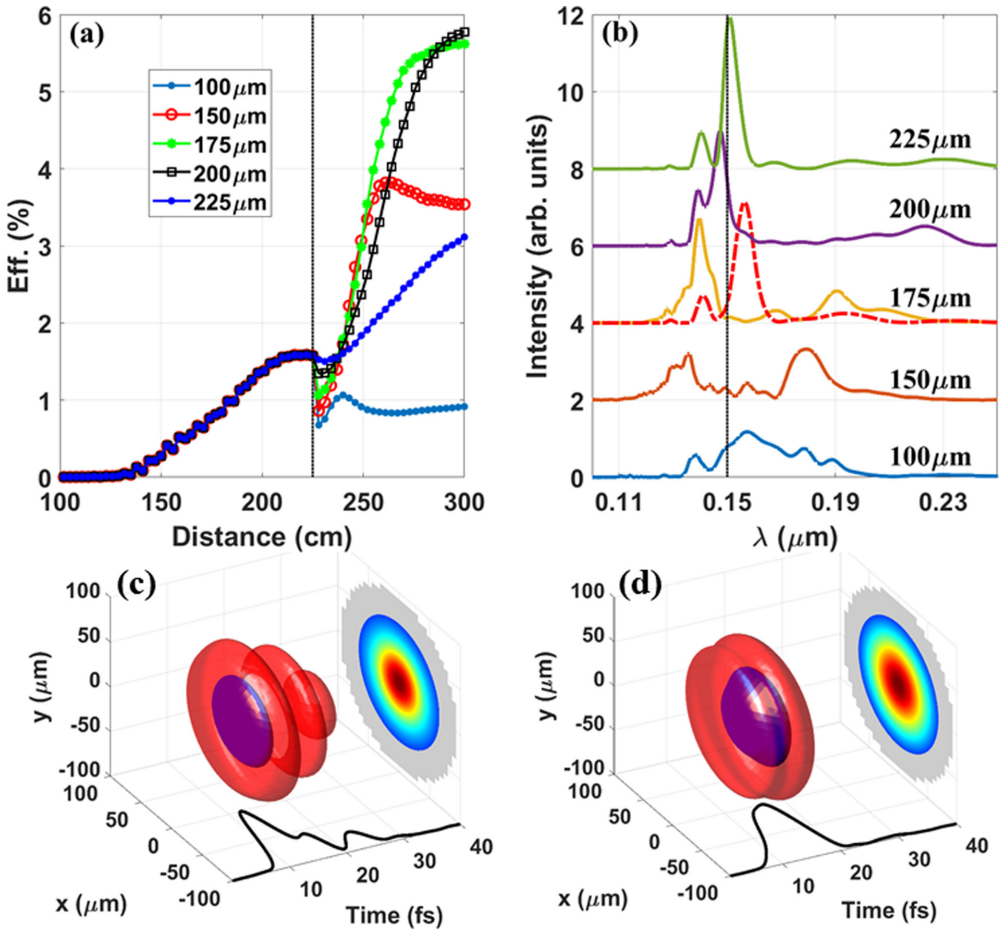

FIG. 4. (a) Evolution of conversion efficiencies of VUV below 150 nm with different core sizes for the second HCF segment, and (b) the final output spectra. The connection location is at 225 cm. The red-dashed line indicates the spectrum obtained with a single 250-μm HCF. (c),(d) Spatiotemporal distributions of the VUV light below 150 nm from the piecewise HCF when the starting location of the second segment is (c) 225 cm and (d) 135 cm. The core size of the second segment is 200 μm. The intensity isosurfaces in blue are 50% of peak intensity, and the red corresponds to 7%. The black lines indicate the temporal intensity profiles on the HCF axis.

Figure 4(a) shows the evolution of CE with different core sizes at 500 mbar. The starting location of the second HCF is 225 cm where the CE in the first segment saturates. After a blocking loss, the CE rises again for core size above 100 μm, with the highest value of 5.5% for 175 and 200 μm. The final spectra are shown in Fig. 4(b). As a comparison, the red-dashed line indicates the unfiltered DW spectrum from a single 250-μm HCF according to the simulations. This spectrum has two peaks. The large peak is above 150 nm; the small one is below 150 nm. The small peak is centered at 142 nm and the CE below 150 nm is 1.7%. In the case of piecewise HCF, the large peak above 150 nm is shifted below 150 nm efficiently when the core size of the second segment is between 175 and 200 μm. Further results show that the CE does not change when the starting location shifts to 180 cm, but is reduced to 4.5% when it shifts to 135 cm where the VUV below 150 nm starts to build up in the first segment. It is found that when the gas pressure is above 450 mbar the VUV below 150 nm in the 250-μm segment mainly concentrates in the EH_{12} mode [35], but in the 200-μm segment it is the EH_{11} mode that achieves the PM condition as shown in Fig. 5. Therefore, the energy enhancement in Fig. 4(a) is in a different spatial mode. The final spatiotemporal distribution of the VUV below 150 nm is shown in Fig. 4(c). As can be seen, different contributions are separated in time domain. To get a clean fundamental mode, the second segment can start at 135 cm. The 4.5% CE still nearly triples the result obtained with a single 250-μm HCF. Figure 4(d) shows the corresponding spatiotemporal distribution. A clean temporal profile is obtained with pulse duration of about 10 fs. It should be noted that the experimental DW spectrum in [12] under the same conditions only shows one peak below 150 nm and the mode is EH_{11} [33], while the numerical simulations here show two peaks [see the dashed line in Fig. 4(b)]. As mentioned in Sec. II, this discrepancy is unclear, and therefore the above analysis is only based on comparison between the numerical simulations. Despite the discrepancy, the structure of multiple bands on multiple modes of DW emission is often observed both numerically and experimentally [12] due to phase matching (PM) at different wavelengths. The piecewise HCF takes advantage of this characteristic to change the PM at specific wavelengths from high-order mode to fundamental mode at proper locations, so that both the conversion efficiency and spatial distribution can be improved.

The CE of a single 3-m HCF with 200 μm core size is 1.8% when the other conditions are kept the same. Using an

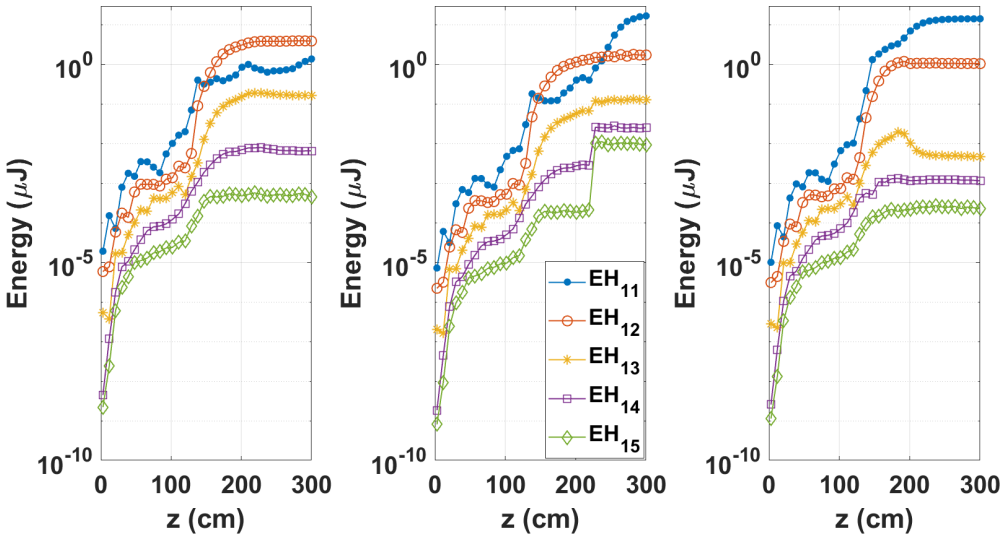

FIG. 5. Evolution of VUV energy below 150 nm on each mode in (a) a single 3-m HCF with 250-μm diameter; (b),(c) a piecewise HCF with 200-μm diameter for the second segment (b) starting at 225 cm and (c) starting at 135 cm. The HCF is filled with 500-mbar helium.

HCF with smaller core size from the start will result in a pulse splitting process due to higher peak intensity, during which a blueshifted soliton is ejected from the main driving pulse and accelerated away, thus reducing the peak power and conversion efficiency. Although the same dynamics can be obtained by simultaneously scaling the energy, pressure, HCF length, and core size according to basic scaling laws [36], the output VUV energy is also greatly reduced. These observations necessitate the use of piecewise HCF for high performance. The performance at 550 mbar is similar to 500 mbar, with the addition that it is also possible to obtain 5.5% CE with a smaller core size (such as 150 μm) of the second segment, even though the range of optimal starting locations is different. The above results show the rich and complex spatiotemporal dynamics of the ultrashort pulses with a supercontinuum from VUV to near infrared in a piecewise HCF, which offers great opportunities to explore for novel applications.

IV. DISCUSSION

One problem about the use of piecewise HCF is the potential damage of high intensity on the fiber clad at the inlet of the second segment with a small core. In the above situation, the peak intensity just before the second 100-μm-core segment is about 3.2×10^{14} W/cm^2 on the edge of the clad as shown in Fig. 6. This intensity is large enough to damage most materials despite its 0.9-fs extreme short duration. In practice, this may lead to a conical transition from 250 to 100 μm in core size due to ablation. The local surface slope of the conical shape determines the intensities imprint on the clad surface. This slope with angle θ from the HCF axis reduces the peak intensity I_{peak} imprint on the clad surface to $I_{\text{peak}} \sin\theta$. If the peak intensity on the clad is reduced to some level (a threshold value), we assume the ablation process stops, and the conical shape is fixed. The exact threshold value is not known. The length of the transition can be estimated to be about 8 cm with a conservative threshold value of 1.0×10^{11} W/cm^2. To estimate the influence on VUV conversion, the core-size transition is approximated by discretization into 16 segments, and the same simulation is performed on this multisegment HCF. The conversion efficiency below 110 nm drops to 0.2%. The efficiency does not change much if the discretization is increased to 32 segments, nor if the threshold intensity is reduced to 5.0×10^{10} W/cm^2. On the other hand, because the tolerance of the inner diameter is from 100 to 150 μm for optimal CE, this loss can be compensated by increasing the core size in the optimal range.

About 20% of input energy is dissipated due to the smallest 100-μm core size. Therefore, how to manage the heat dissipation in the practice will require engineering efforts. For the enhancement of VUV below 150 nm with 200 μm core size, the damage and heat dissipation do not cause problems.

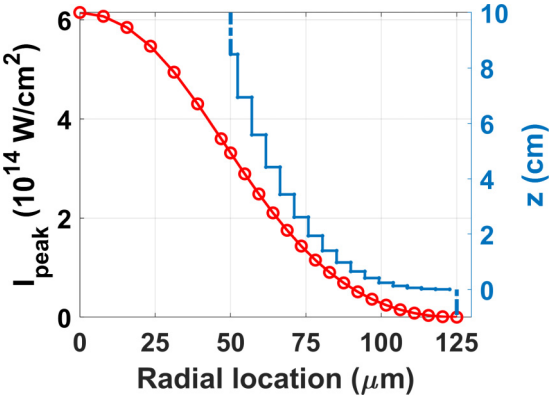

FIG. 6. Peak intensities along the radial direction in the 250-μm HCF before the pulse enters the 100-μm HCF (red-circle line). The fiber clad of the 100-μm HCF can be ablated by the pulse, and the core size can form a curved conical transition from 250 to 100 μm. The hollow-core size of the transition is determined by the intensity threshold imprint on the clad surface. The blue-dotted line indicates the transition profile approximated by discretization into 16 segments. The intensity threshold is chosen to be 1.0×10^{11} W/cm^2.

To prepare the piecewise HCF, an alignment beam is needed. The first segment is aligned with the beam to obtain a high transmission efficiency with the fundamental mode. Then the second segment is placed following the first one and is also adjusted for a high efficiency. There can be a gap between the two segments. According to simulations, the beam can propagate in free space between the two segments up to 5 mm without obvious expansion. After alignment, the two segments can be fixed to a common element on the outside with glue. This way of making a piecewise HCF can also solve the practical issue with the lack of suitable gas cell window materials for wavelengths below 110 nm. For example, an extra segment can be added to channel the VUV pulse to the vacuum output end through pressure gradient configuration.

V. CONCLUSION

This work investigated a method using a piecewise HCF in order to push the shortest VUV DW emission below 110 nm efficiently. Through rigorous numerical simulations and quantitative analysis, it is found that a coherent VUV source from 90 to 110 nm with microjoule-level pulse energy can be obtained if the various parameters of the system are properly designed and matched. According to the simulation results, the piecewise HCF can also significantly enhance the CE of VUV below 150 nm as well as improve the spatiotemporal distribution profile of the output. The rich and complex propagation dynamics are revealed, and the optimal experimental conditions are identified in the large parameter space. As a result, the whole VUV spectrum can now be accessed efficiently, with single pulse energy of microjoule level. The unique features, such as wavelength tunability, broadband spectrum, and femtosecond duration, can offer new research opportunities in various areas requiring VUV sources.

On the other hand, the piecewise gas-filled HCFs offer the flexibility of tuning the dispersion profile in radical ways, and also facilitate the change of gas species in the HCFs in compact manners without the beam leaving the HCF and reentering another HCF. These advances can take relevant research to a new level, opening up many possibilities waiting for exploration.

ACKNOWLEDGMENTS

The authors acknowledge support from National Natural Science Foundation of China (NSFC) (Grants No. 61521093, No. 61925507, No. 61635012, and No. 11604351), National Key Research and Development Program of China (Grant No. 2017YFE0123700), Program of Shanghai Academic/Technology Research Leader (Grant No. 18XD1404200), Strategic Priority Research Program of the Chinese Academy of Sciences (Grant No. XDB1603), Major Project Science and Technology Commission of Shanghai Municipality (STCSM) (Grant No. 2017SHZDZX02). The authors thank the anonymous reviewers for helping to improve the manuscript.

[1] E. van Dishoeck, E. Herbst, and D. Neufeld, Interstellar water chemistry: From laboratory to observations, Chem. Rev. **113**, 9043 (2013).

[2] Y. Chang, Y. Yu, H. Wang, X. Hu, Q. Li, J. Yang, S. Su, Z. He, Z. Chen, L. Che, X. Wang, W. Zhang, G. Wu, D. Xie, M. Ashfold, K. Yuan, and X. Yang, Hydroxyl super rotors from vacuum ultraviolet photodissociation of water, Nat. Commun. **10**, 1250 (2019).

[3] H. Gao, Molecular photodissociation in the vacuum ultraviolet region implications for astrochemistry and planetary atmospheric chemistry, Mol. Phys. **119**, e1861354 (2021).

[4] S. Souma, T. Sato, T. Takahashi, and P. Baltzer, High-intensity xenon plasma discharge lamp for bulk-sensitive high-resolution photoemission spectroscopy, Rev. Sci. Instrum. **78**, 123104 (2007).

[5] R. Mota, R. Parafita, A. Giuliani, M. Hubin-Franskin, J. Lourenco, G. Garcia, S. Hoffmann, N. Mason, P. Ribeiro, M. Raposo, and P. Limao-Vieira, Water VUV electronic state spectroscopy by synchrotron radiation, Chem. Phys. Lett. **416**, 152 (2005).

[6] Y. Chang, S. Yu, Q. Li, Y. Yu, H. Wang, S. Su, Z. Chen, L. Che, X. Wang, W. Zhang, D. Dai, G. Wu, K. Yuan, and X. Yang, Tunable VUV photochemistry using vacuum ultraviolet free electron laser combined with H-atom Rydberg tagging time-of-flight spectroscopy, Rev. Sci. Instrum. **89**, 063113 (2018).

[7] J. J. Ewing, Excimer laser technology development, IEEE J. Sel. Top. Quantum Electron. **6**, 1061 (2000).

[8] L. Kang and Z. Lin, Deep-ultraviolet nonlinear optical crystals: Concept development and materials discovery, Light: Sci. Appl. **11**, 201 (2022).

[9] Z. Li, L. Yan, P. Zuo, L. Xie, Z. Li, and B. Jin, Development of Tabletop Femtosecond Vacuum Ultraviolet Laser Source Based on Four-Wave Mixing Techniques, Chin. J. Lasers **48**, 1201007 (2021).

[10] B. Jones, J. Zhou, L. Yang, and C. Ng, High-resolution Rydberg tagging time-of-flight measurements of atomic photofragments by single-photon vacuum ultraviolet laser excitation, Rev. Sci. Instrum. **79**, 123106 (2008).

[11] D. Albert, D. Proctor, and H. Davis, High-intensity coherent vacuum ultraviolet source using unfocussed commercial dye lasers, Rev. Sci. Instrum. **84**, 063104 (2013).

[12] J. Travers, T. Grigorova, C. Brahms, and F. Belli, High-energy pulse self-compression and ultraviolet generation through soliton dynamics in hollow capillary fibers, Nat. Photonics **13**, 547 (2019).

[13] A. Lekosiotis, C. Brahms, F. Belli, T. Grigorova, and J. Travers, Ultrafast circularly polarized pulses tunable from the vacuum to deep ultraviolet, Opt. Lett. **46**, 4057 (2021).

[14] C. Brahms, F. Belli, and J. Travers, Resonant dispersive wave emission in hollow capillary fibers filled with pressure gradients, Opt. Lett. **45**, 4456 (2020).

[15] P. Russell, P. Holzer, W. Chang, A. Abdolvand, and J. Travers, Hollow-core photonic crystal fibres for gas-based nonlinear optics, Nat. Photonics **8**, 278 (2014).

[16] N. Joly, J. Nold, W. Chang, P. Holzer, A. Nazarkin, G. Wong, F. Biancalana, and P. Russell, Bright Spatially Coherent Wavelength-Tunable Deep-Uv Laser Source Using an Ar-Filled Photonic Crystal Fiber, Phys. Rev. Lett. **106**, 203901 (2011).

[17] P. Holzer, W. Chang, J. Travers, A. Nazarkin, J. Nold, N. Joly, M. Saleh, F. Biancalana, and P. Russell, Femtosecond Nonlinear Fiber Optics in the Ionization Regime, Phys. Rev. Lett. **107**, 203901 (2011).

[18] M. Saleh, W. Chang, P. Holzer, A. Nazarkin, J. Travers, N. Joly, P. Russell, and F. Biancalana, Theory of Photoionization-Induced Blueshift of Ultrashort Solitons in Gas-Filled Hollow-Core Photonic Crystal Fibers, Phys. Rev. Lett. **107**, 203902 (2011).

[19] L. Wright, S. Wabnitz, D. Christodoulides, and F. Wise, Ultrabroadband Dispersive Radiation by Spatiotemporal Oscillation of Multimode Waves, Phys. Rev. Lett. **115**, 223902 (2015).

[20] N. Axelrod and M. Givens, Absorption of gaseous helium in the extreme ultraviolet, Phys. Rev. **115**, 97 (1959).

[21] M. Erkintalo, Y. Xu, S. Murdoch, J. Dudley, and G. Genty, Cascaded Phase Matching and Nonlinear Symmetry Breaking in Fiber Frequency Combs, Phys. Rev. Lett. **109**, 223904 (2012).

[22] C. Brahms, T. Grigorova, F. Belli, and J. Travers, High-energy ultraviolet dispersive-wave emission in compact hollow capillary systems, Opt. Lett. **44**, 2990 (2019).

[23] C. Brahms, F. Belli, and J. Travers, Infrared attosecond field transients and UV to IR few-femtosecond pulses generated by high-energy soliton self-compression, Phys. Rev. Res. **2**, 043037 (2020).

[24] T. Popmintchev, M. Chen, D. Popmintchev, P. Arpin, S. Brown, S. Alisauskas, G. Andriukaitis, T. Balciunas, O. Mucke, A. Pugzlys, A. Baltuska, B. Shim, S. Schrauth, A. Gaeta, C. Hernandez-Garcia, L. Plaja, A. Becker, A. Jaron-Becker, M. Murnane, and H. Kapteyn, Bright Coherent Ultrahigh Harmonics in the keV X-ray Regime from Mid-Infrared Femtosecond Lasers, Science **336**, 1287 (2012).

[25] R. Safaei, G. Fan, O. Kwon, K. Legare, P. Lassonde, B. Schmidt, H. Ibrahim, and F. Legare, High-energy multidimensional solitary states in hollow-core fibres, Nat. Photonics **14**, 733 (2020).

[26] R. Piccoli, J. Brown, Y. Jeong, A. Rovere, L. Zanotto, M. Gaarde, F. Legare, A. Couairon, J. Travers, R. Morandotti, B. Schmidt, and L. Razzari, Intense few-cycle visible pulses directly generated via nonlinear fiber mode mixing, Nat. Photonics **15**, 884 (2021).

[27] M. Muller, C. Aleshire, A. Klenke, E. Haddad, F. Legare, A. Tunnermann, and J. Limpert, 10.4 kW coherently combined ultrafast fiber laser, Opt. Lett. **45**, 3083 (2020).

[28] J. Andreasen and M. Kolesik, Mid-infrared femtosecond laser pulse filamentation in hollow waveguides: A comparison of simulation methods, Phys. Rev. E **87**, 053303 (2013).

[29] J. Andreasen and M. Kolesik, Nonlinear propagation of light in structured media: Generalized unidirectional pulse propagation equations, Phys. Rev. E **86**, 036706 (2012).

[30] M. Kolesik and J. V. Moloney, Nonlinear optical pulse propagation simulation: From Maxwell's to unidirectional equations, Phys. Rev. E **70**, 036604 (2004).

[31] A. M. Perelomov, V. S. Popov, and M. V. Terent'ev, Ionization of atoms in an alternating electric field, Sov. Phys. JETP **23**, 924 (1966).

[32] R. Kitamura, L. Pilon, and M. Jonasz, Optical constants of silica glass from extreme ultraviolet to far infrared at near room temperature, Appl. Opt. **46**, 8118 (2007).

[33] Pointed out by the anonymous reviewer.

[34] A. Ermolov, K. Mak, M. Frosz, J. Travers, and P. Russell, Supercontinuum generation in the vacuum ultraviolet through dispersive-wave and soliton-plasma interaction in a noble-gas-filled hollow-core photonic crystal fiber, Phys. Rev. A **92**, 033821 (2015).

[35] F. Tani, J. C. Travers, and P. St. J. Russell, Multimode ultrafast nonlinear optics in optical waveguides: Numerical modeling and experiments in kagome photonic-crystal fiber, J. Opt. Soc. Am. B **31**, 311 (2014).

[36] C. Heyl, H. Coudert-Alteirac, M. Miranda, M. Louisy, K. Kovacs, V. Tosa, E. Balogh, K. Varju, A. L'Huillier, A. Couairon, and C. L. Arnold, Scale-invariant nonlinear optics in gases, Optica **3**, 75 (2016).